Supporting Information

Botter et al. 10.1073/pnas.1311920110

SI Materials and Methods

In this section, additional information is provided on the methods used in the paper to characterize the river flow regimes and their exposure/sensitivity to climate change.

Analytical Characterization of the Flow Regime. The basis of the analytical model on which the classification of flow regimes proposed in the paper is built is a stochastic description of daily stream flow dynamics, which are assumed to result from the superposition of a sequence of flow pulses triggered by precipitation. In particular, the sequence of streamflow-producing rainfall events during a given season is assumed to be a suitable subset of the overall rainfall. This subset, often termed excess precipitation, is created by the events bringing enough water to fill the soil–water deficit resulting from plant transpiration, driving the soil moisture in the unsaturated region above the field capacity. The overall rainfall forcing can typically be assimilated to a marked Poisson process with frequency λ_p and to exponentially distributed depths with average α (1). As a consequence, the sequence of events producing streamflows can also be approximated by a Poisson process similar to the main rainfall, although characterized by a reduced frequency, $\lambda < \lambda_p$ (2). The ratio λ/λ_p expresses the ability of the near-surface soil moisture to filter the incoming rainfall forcing, and it can be analytically expressed as a function of climate, soil, and vegetation attributes (Eq. **S3**). When precipitation determines an excess of water in the root zone, such excess water is eliminated through the catchment hydrological response. If the subsurface catchment storage is assumed to behave like a linear reservoir with time constant k, each pulse determines a sudden increase of the stream flow followed by an exponential-like recession.

In mathematical terms, a pulse with an excess depth $h_i[L]$ released at time t_i from the root zone provides a contribution to the overall specific (per unit catchment area) streamflow, Q, which is equal to $h_i\ k\ \exp\ [-k(t-t_i)]$. Hence, the instantaneous streamflow increment determined by the above water flow impulse at the time when the pulse is produced from the root zone (i.e., for $t=t_i$) is kh_i (i.e., $k \times$ pulse depth). Provided that the system is linear, the overall streamflow is just the sum of the contribution of the different effective pulses taking place, and the presence of overlapping pulses does not change the recession time constant. Hence, the stochastic dynamical equation for $Q(t)$ at a daily time scale is (2):

$$\frac{dQ(t)}{dt} = -k\ Q(t) + \xi_t, \qquad \text{[S1]}$$

where the first term on the right-hand side expresses the exponential decay of the flow between the events and the second term ($\xi_t[L/T^2]$) formally embeds the series of stochastic jumps induced on Q by the sequence of flow pulses. Given the assumptions made on the pulse occurrences, the flow-producing events have instantaneous durations (i.e., ξ_t is different from zero only during a set of finite times) and produce a sequence of positive jumps in the dynamics of Q. The "Poissonianity" of the events also implies that the interarrival times between these jumps are exponentially distributed with mean $1/\lambda$. Given the exponential distribution of the rainfall depths, the extents of the jumps experienced by Q are random and exponentially distributed with mean $k\alpha$ ($k \times$ pulse depth). Under these assumptions, the master equation associated with the probability density function (pdf) of the flow Q at time t, $p(Q,t)$, reads (2, 3):

$$\frac{\partial p(Q,t)}{\partial t} = \frac{\partial [k\ Q\ p(Q,t)]}{\partial Q} - \lambda p(Q,t) + \frac{\lambda}{\alpha k}\int_0^Q p(Q-z,t)\exp[-z/(\alpha k)]\,dz. \qquad \text{[S2]}$$

The steady-state pdf of the specific river discharge is thus given by the solution of the master equation for $t \to \infty$, which leads to Eq. **2**. The steady-state mean and variance of the process are $\lambda\ \alpha$ and $\lambda\ k\ \alpha^2$ (respectively), implying that the coefficient of variation of daily flows (CV_Q) is $\sqrt{k/\lambda}$. Despite the fact that some of the related hydrological processes are somewhat simplified (e.g., rainfall dynamics, hydrological response of the catchment) and other processes are completely disregarded (e.g., geomorphological and hydrodynamic dispersion in the river network), the above approach provides a robust linkage between the river flow regime and a few (directly measurable) rainfall and landscape attributes of the contributing catchment. The model was able to predict the observed frequency distribution of river discharges in many temperate catchments of the Alps and the United States successfully under a range of climate and morphological conditions (4, 5).

Catchment Selection. In this study, 44 different catchments with synchronous discharge and rainfall records were selected to analyze their flow regime and investigate the flow regime variability on different temporal scales. The study catchments are scattered throughout the United States and the Alps so as to cover a wide range of hydrological and climatic conditions. Thirty-two catchments are located in the United States, whereas the remaining watersheds are located in the Italian Alps. Hydrological and climatic records have been collected by the Regional Agency for Environmental Protection of the Veneto Region and by the US Geological Survey (http://waterdata.usgs.gov) and the National Climatic Data Center (http://cdo.ncdc.noaa.gov/). The size of the catchments spanned one order of magnitude (from 10 to 10^3 km^2), a range within which the characterization of the flow regime through spatially averaged parameters proved meaningful (4, 5). The seasons of the year were identified on the basis of calendar dates (spring: 03/01–05/31, summer: 06/01–08/31, fall: 09/01–11/30, and winter: 12/01–02/28). In the selection, highly engineered rivers characterized by anthropogenic regulation were excluded from the analysis, as well as snow-impacted regimes observed in cases of intense snow melting or accumulation. In particular, all the combinations of catchments/seasons for which the snow input was greater than 70% of the overall input (rain and snow) were assumed to be affected by snow accumulation processes and discarded. Similarly, cases in which the mean rainfall was found to be equal to (or smaller than) the mean streamflow were considered to be affected by melting processes and discarded. The overall number of catchments/seasons combinations considered in this study was 110. Additional information on the selected catchments and the datasets used is provided in Table S1.

Parameter Identification. The analytical model identifies three major parameters as the primary controls on the flow regime: (*i*) the recession time constant, k; (*ii*) the mean depth of rainfall events, α; and (*iii*) the frequency of streamflow-producing events, λ. These three parameters could be estimated from hydrological and climatic data, as detailed below.

The mean depth of rainfall events, α, can be computed from rainfall records as the observed mean daily depth during wet

days. The average frequency of streamflow-producing events, λ, can be estimated exploiting the crossing properties of soil moisture from the frequency of daily rainfall, λ_p, and other climate/soil/vegetation parameters (1, 6) as:

$$\lambda = \eta \frac{\exp\left(-\beta^{-1}\right)\beta^{-\frac{\lambda_p}{\eta}}}{\gamma\left(\lambda_p/\eta, \beta^{-1}\right)}, \qquad \textbf{[S3]}$$

where $\gamma(a,b)$ is the lower incomplete Gamma-function of parameters a and b, whereas η and β are the mean transpiration rate and the mean rainfall depth (both normalized to the depth of water available to plants in the root zone), respectively. The parameter k, which represents the inverse of the time scale of the hydrograph, could be obtained through morphological and pedological features (e.g., by dividing the mean length of unchanneled paths by a scale velocity representing the mean hydraulic conductivity of subsurface environments).

However, to make the estimation of λ and k easier, and to allow for their calculation in case of missing landscape information, λ and k have been estimated in this paper by combining rainfall and streamflow data. In particular, λ is estimated by equalling the observed mean specific discharge, $\langle Q \rangle$, and the analytical mean of Q according to the stochastic model (i.e., $\lambda = \langle Q \rangle / \alpha$). The consistency of the estimate of λ has been verified through the comparison of theoretical and observed pdfs and by comparing the estimated value of λ with the rainfall frequency λ_p (which is derived by comparing the probability distribution of the number of wet days in a reference time period and the corresponding Poisson pdf assumed by the rainfall model; Fig. S1*A*). Note that in Alpine catchments, to account for the marked heterogeneity of rainfall fields, rainfall analyses were performed using spatially averaged daily precipitation rates obtained by averaging the records available in all the precipitation stations located within or nearby the considered catchments. In the remaining study catchments, instead, due to the enhanced uniformity of rainfall and to exploit as much as possible the long-term flow records available, we considered only the station with the longest rainfall record among the available meteorological stations. The robustness of the estimate performed has then been verified a posteriori by comparing the estimates made using a single station and those obtained with multiple stations during selected periods in which synchronous precipitation measurements in different stations are available. The recession rate, k, is derived instead from observed streamflows through a regression analysis [i.e., a linear regression between the estimated temporal derivatives of Q (dQ/dt) and the corresponding observed discharges (7)]. To exclude the effect of fast flows, which have a limited impact on the flow distribution (especially on daily time scales) but may significantly constrain the regression, only the discharges falling within the 0.9 quantile of the distribution are considered.

An example of the estimation procedure based on rainfall and discharge data for the Drowning Creek catchment is illustrated in Fig. S1. In particular, Fig. S1*A* compares the probability distribution of the number of wet days observed in a reference time period in a gauging station chosen among those used in the study and the corresponding Poisson pdf assumed by the rainfall model. The procedure is used to estimate the rainfall frequency, λ_P, which is used as a term of comparison for the estimated values of λ. Similarly, Fig. S1*B* shows the comparison between the observed distribution of the daily depths and the exponential distribution assumed by the analytical model. A relevant example of regression analysis is presented in Fig. S1*C*. Despite the observed scattering, which has an impact on only the higher order moments of the flow pdf (8), the procedure allowed an objective description of the heterogeneity in the hydrological response of the study catchments (Fig. 1).

To assess the robustness of the estimation procedure based on rainfall and streamflow data for a selected catchment chosen among the available sites (the Boite River at Cancia), we have performed an independent estimate of the parameters λ and k based only on climate and landscape data. In particular, λ has been estimated by means of Eq. **S3** using only climatic, soil, and soil-use data, which are necessary to calculate the parameters η and β (4). The soil parameters have been determined based on the literature (5), whereas the potential evapotranspiration rate, on which η depends, has been obtained by multiplying a crop coefficient, Kc (estimated on the basis of the soil cover), and the reference potential evapotranspiration estimated based on temperature data using the Blaney–Criddle equation. Furthermore, the interannual average of k has been estimated as the ratio between the mean length of unchanneled paths (calculated from a digital terrain map) and the mean hydraulic conductivity (estimated based on the soil type distribution in the catchment). Then, the interannual variability of k has been linked to the interannual variability of the mean rainfall intensity, assuming that k is proportional to the corresponding mean rainfall depth during each period. Fig. S2 shows a comparison between the estimated values of the hydroclimatic parameters λ, k, and α obtained using climate and landscape attributes and those obtained from both rainfall and streamflow data. The two methods provide significantly similar results, also in terms of sensitivity, exposure, regime instability, and λ/k ratio, reinforcing the robustness of the estimation method used in the paper.

Model Performances. The streamflow pdf predicted by the analytical model has then been compared with the observed frequency distribution of daily flows for all the selected combinations of catchments/seasons. The comparison has been undertaken for the whole period of record and for consecutive nonoverlapping periods of 2 and 8 y contained within each dataset. The parameters of the flow pdf have been estimated coherently from the available observations for each time span. Relevant examples of the fitting between the stochastic analytical model and the observed river flow pdfs are reported in Fig. S3. A summary of the model performances is shown in Fig. S3*A* through the pdf of the (percentage) integral error between the analytical and observed flow pdfs, calculated as the cumulative error in the probability, which is attributed by the analytical model to the N intervals of amplitude, ΔQ, used to characterize the frequency distribution of the observed flows:

$$\varepsilon = \frac{1}{2}\sum_{i}^{N}\left|\frac{n_i}{m} - \frac{\Gamma\left[\lambda/k, Q_i/(\alpha k)\right] - \Gamma\left[\lambda/k, (Q_i+\Delta Q)/(\alpha k)\right]}{\Gamma[\lambda/k]}\right|, \qquad \textbf{[S4]}$$

where $Q_1 = 0$, $Q_i = Q_{i-1} + \Delta Q$ $(i > 1)$, and n_i represent the number of observed streamflows falling in the interval $[Q_i, Q_i + \Delta Q]$ (among the m data available during the considered period). On the 8-y time scale, 90% of the cases analyzed are characterized by a percentage areal error, ε, less than 30%. The performance of the model obviously decreases when shorter time spans are considered (60% of the cases with an error smaller than 30% for the 2-y regimes), possibly due to the limited ergodicity of the time series at those time scales. Overall, the performances of the model are judged satisfactory, especially in view of the simplicity of the model and the limited number of parameters (which were not calibrated but only calculated from available hydrological data). In selected case studies, in which both daily and subdaily flow data were available, we have also checked the robustness of the results obtained in the paper in comparison to the underlying temporal scale of the data used by comparing the pdf of the daily streamflow and the pdf of the streamflows evaluated at subdaily time scales. In none of the cases analyzed has the temporal resolution been found to have a significant impact on the result. As an example, Fig. S4 shows

the comparison between the daily and 15-min streamflow pdfs in the Flat Creek (NC), which is one of the smallest catchments considered in the study (and where the effect of subdaily streamflow dynamics is thus enhanced). Regardless of the season considered, and regardless of the type of regime, the observed impact of the temporal resolution of data on the flow pdf is negligible, reinforcing the robustness of the approach used in the study.

Flow Regimes and Mean Specific Discharge. Although the type of flow regime has been found to be almost independent of the underlying precipitation pattern, the nature of the regime is quite strongly correlated with the mean specific (per unit catchment area) discharge, $\langle Q \rangle$. In particular, Fig. S5 shows that the mean specific discharge sensibly decreases with the CV_Q, clearly suggesting that erratic regimes are infrequent in rivers with specific discharges larger than 0.1 cm/d. On the other hand, a large majority of the cases where $\langle Q \rangle < 0.1$ cm/d are found to be erratic (but not vice versa), thereby suggesting that low $\langle Q \rangle$ may represent a sufficient but not necessary condition for the erraticity of the regime.

Exposure Index. According to the analytical model, the streamflow pdf is a Gamma-distribution with shape parameter $s = \lambda/k$ and rate parameter $r = \alpha k$. Hence, in this framework, the variability of the flow regime across different periods is related to the variability of the shape and rate parameters of the Gamma-pdf, which is, in turn, induced by the interannual fluctuations of λ, α, and k. Such fluctuations were found to be weakly correlated ($\rho_{\lambda,k} = 0.21$, $\rho_{\lambda,\alpha} = 0.04$, and $\rho_{\alpha,k} = 0.31$) and quite significant at all the time scales, especially for the frequency of the events (with an average coefficient of variation of λ close to 0.96). On this basis, the exposure to climate change of the flow regime was estimated for each catchment and season through the exposure index (E), defined as the sum of the modulus of the relative variations of the shape and rate parameters of the Gamma-pdf in Eq. **2**:

$$E = \left|\frac{\Delta s}{s}\right| + \left|\frac{\Delta r}{r}\right|. \qquad \textbf{[S5]}$$

Eq. **S5** incorporates the overall variability induced by hydroclimatic fluctuations in the ratio λ/k and in the product αk, properly discounting the self-compensating changes in the number, persistency, and intensity that maintain unaltered the flow pdf (e.g., simultaneous increases of λ and k maintaining unaltered the ratio λ/k, and thus the type of regime). Note that the right-hand side of Eq. **S5** is the sum of two moduli; hence, possible tradeoffs related to contrasting changes of the shape and rate parameters (e.g., r increasing and s decreasing) are not considered. The E has been computed for each catchment/season by calculating the relative variations of r and s across all the nonoverlapping groups of 2 and 8 y contained in the datasets. Note that for the analysis of the 8-y regimes, only catchments with at least 50 y of data were considered.

Regime Instability Index. The regime instability is quantified through the regime instability index (RI), which is defined by the integral of the modulus of the difference between the river flow pdfs pertaining to two distinct periods [$p_1(Q)$ and $p_2(Q)$]:

$$RI = 0.5 \int_0^\infty |p_2(Q) - p_1(Q)| dQ. \qquad \textbf{[S6]}$$

The RI is thus bounded between 0 and 1, where $RI = 0$ implies that the flow regimes in the considered periods are perfectly overlapping (long-term stability of the flow regime) and $RI = 1$ implies disjoint river flow pdfs (a radical change of the flow regime, where all the flows recorded during the first period are not observed in the second period, and vice versa). The RI properly summarizes the volatility of the flow regime across different years, including high/low-flow frequencies, modal flows, and intraseasonal flow variability. Fluctuations in the temporal correlation of the flows are instead disregarded. The numerical computation of the RI from observed discharges poses serious challenges due to the strong dependence of the result on the integration interval, ΔQ. When ΔQ is large, the RI is artificially small because of the enhanced smoothing of the resulting estimates of p_1 and p_2 (Fig. S6). On the contrary, when the sampling interval ΔQ is too small, the RI tends to be artificially large because of the huge fluctuations of the pdfs. To overcome this difficulty, we have computed the integral of Eq. **S5** using a number of flow intervals, N, ranging from 1 to 500. The behavior of the RI as a function of N has then been analyzed. For the reasons discussed above, the RI was generally found to be a growing function of N; however, in most cases, it presents a stable plateau (i.e., similar values of RI within a range of N). The regime instability index RI is calculated as the average of the function $RI(N)$ calculated within the observed plateau, thereby assuming that the independence of RI on N indicates that the corresponding ΔQ values used for the numerical integration are large enough to limit the effect of fluctuations in the sampling of the flow pdfs but small enough to capture the behavior of the flow regimes in the two periods (Fig. S6). The cases where the function $RI(N)$, after the application of a suitable moving average aimed at removing the high-frequency fluctuations, does not display a range of 50 consecutive values of N with nearly constant values of the RI (at most $\pm 5\%$ of the initial value) were disregarded. The procedure has been repeated for all the combinations of catchments/seasons and for all the periods of 2 and 8 y available in each dataset. Different ways of computing the integral in Eq. **S6** (e.g., by using a fixed number of classes or classes with an amplitude proportional to the mean discharge) provide results that are qualitatively analogous to those shown in Fig. 3.

Sensitivity to Climate Change. The sensitivity, S, of the flow regime to climate changes is computed as the ratio between the regime instability and the exposure. High sensitivities imply that the underlying hydroclimatic fluctuations produce amplified effects in the flow regime, with relevant changes in the frequencies associated with discharges of any size. It should be emphasized, however, that the regime instability cannot be entirely related to interannual fluctuations of the number, persistency, and mean intensity of the flow pulses. In fact, regime instability may also arise due to, for example, changes in the temporal distribution of the events, lack of ergodicity within the considered periods, and interannual variability of processes that are not explicitly included in the analytical model. As a result, in a few cases, the calculated value of the RI was found to be much larger than the corresponding exposure (mainly because of the constancy of λ, α, and k). This leads to overestimated values of the sensitivity, which, however, mirror only the circumstantial stability of λ, α, and k and emphasize the role of second-order processes (e.g., episodic snowfalls, untracked changes in the stage-discharge relation) whose effect on the flow regime is typically beclouded. To focus on the role played by the interannual fluctuations of the number, persistency, and mean intensity of the flow pulses, we have thus disregarded all the cases in which the estimated exposure was lower than 0.1, assuming that the related estimates of the sensitivity could not be reliable below this threshold. Were these points included, the main conclusions of the paper would remain unaltered, with the major consequence being an increased scattering of the points in Fig. 3*C*. The sensitivity of the flow regime to climate changes can also be characterized analytically using the stochastic analytical model embedded in Eq. **2**. The change of probability density associated with any discharge of size Q (between the periods 1 and 2) can be approximated using a first-order Taylor series expansion as:

$$\Delta p(Q) \simeq \frac{\partial p}{\partial s}\Delta s + \frac{\partial p}{\partial r}\Delta r, \qquad \textbf{[S7]}$$

where Δr and Δs are the variations of shape and rate parameters of the flow pdf in the considered periods. Hence, the RI can be expressed using Eqs. **S6** and **S7** as:

$$RI = 0.5 \int_0^\infty |\Delta p(Q)| dQ \simeq$$
$$\simeq 0.5 \int_0^\infty \left| \Delta s \left(\frac{\partial p(Q)}{\partial s} \right) + \Delta r \left(\frac{\partial p(Q)}{\partial r} \right) \right| dQ. \quad \textbf{[S8]}$$

If we further assume that the functions $\frac{\partial p}{\partial s}$ and $\frac{\partial p}{\partial r}$ have the same sign for all the values of Q (which proves nearly true in most cases), and if we focus only on the cases where the changes of s and r are in concordance (so that Δs and Δr have the same sign), Eq. **S8** can be rewritten as follows:

$$RI \simeq \left| \frac{\Delta s}{s} \right| \int_0^\infty \frac{s}{2} \left| \frac{\partial p(Q)}{\partial s} \right| dQ +$$
$$+ \left| \frac{\Delta r}{r} \right| \int_0^\infty \frac{r}{2} \left| \frac{\partial p(Q)}{\partial r} \right| dQ \quad \textbf{[S9]}$$
$$= \left| \frac{\Delta s}{s} \right| f_s(s) + \left| \frac{\Delta r}{r} \right| f_r(s),$$

where $f_s(s)$ and $f_r(s)$ are suitable dimensionless functions of the ratio λ/k, whose analytical expressions are given by:

$$f_r(s) = \frac{\exp(-s)\, s^s}{\Gamma(s)}, \quad \textbf{[S10]}$$

$$f_s(s) = \frac{s}{2\,\Gamma(s)} G_{2,3}^{3,0} \left(\psi_0(s) \middle| \begin{matrix} 1, 1 \\ 0, 0, s \end{matrix} \right), \quad \textbf{[S11]}$$

where $\psi_0(s)$ is the Digamma-function and G is the Meijer G-function. From Eq. **S9**, the following expression of the sensitivity is finally obtained:

$$S = \frac{RI}{E} = E_s f_s(s) + [1 - E_s] f_r(s), \quad \textbf{[S12]}$$

where $E_s = |\Delta s|/(sE)$ represents the contribution of the variability of λ/k to the overall exposure. Eq. **S12** shows that the sensitivity is a weighted average of f_s and f_r, which are both monotonic increasing functions of s.

Hypothesis Testing. The diverse degree of exposure and sensitivity of the two regime types has been quantitatively assessed using some hypothesis testing based on the distribution of the values of E and S of the cases classified as persistent and erratic (intermediate regimes have been excluded from the analysis). We first tested the hypothesis of normality of the two samples using a Lilliefors test, which was indeed accepted at the 5% significance level for both of the variables $\langle E \rangle$ and $\langle S \rangle$ at both of the considered time scales (2 and 8 y). Then, a standard t test was used to assess the different mean sensitivity and exposure of the two groups. The test was performed formulating the null hypothesis that E and S in erratic and persistent regimes have the same mean with unknown variances. For all the cases analyzed, the null hypothesis was rejected at $P < 0.05$, thereby implying that the exposure $\langle E \rangle$ and the sensitivity $\langle S \rangle$ of erratic and persistent rivers are statistically different (Fig. 3).

SI Discussion

Eqs. **S10**–**S12** show that sensitivity is mainly a function of the ratio $s = \lambda/k$, implying that the sensitivity is directly related to the intraseasonal flow variability, $CV_Q = s^{-1/2}$, as also suggested by observational data. Fig. 3*C* (*Inset*) shows a comparison between the observed sensitivity between all the pairs of 2-y periods characterized by concordant changes of s and r, and the theoretical lines given by Eqs. **S10** and **S11**, where s is expressed as a function of CV_Q via $s = CV_Q^{-2}$. Despite the scattering of the data, the agreement with the theoretical pattern is remarkable. The observed reduced sensitivity to climate change of erratic flow regimes is thus also explained theoretically by the nature of the frequency distribution of river flows. The reduced sensitivity of erratic regimes can also be explained on physical grounds as follows. The reduced flow variability associated with persistent regimes is guaranteed by the occurrence of a sufficient number of events bringing a suitably continuous water supply to the river. As such, persistent regimes are more sensitive to changes in precipitation features (λ, α) with respect to erratic regimes, where the presence of stream water is primarily related to the ability of catchments to modulate the release of water stored in the subsurface. Hence, erratic regimes are more sensitive to changes in the features of the hydrological response, k. Any variation of k, however, entails a simultaneous and concordant change in the shape and rate parameters of the flow pdf, leading to a tradeoff that decreases the variability of the flow pdf and reduces the RI.

1. Rodriguez-Iturbe I, Porporato A, Ridolfi L, Isham V, Cox DR (1999) Probabilistic modelling of water balance at a point: The role of climate, soil and vegetation. *Proc R Soc Lond A Math Phys Sci* 455(1990):3789–3805.
2. Botter G, Porporato A, Rodriguez-Iturbe I, Rinaldo A (2007) Basin-scale soil moisture dynamics and the probabilistic characterization of carrier hydrologic flows: Slow, leaching-prone components of the hydrologic response. *Water Resour Res* 43(2): W02417.
3. Gardiner CW (2004) *Handbook of Stochastic Methods for Physics, Chemistry and the Natural Sciences* (Springer, Berlin).
4. Botter G, Peratoner F, Porporato A, Rodriguez-Iturbe I, Rinaldo A (2007) Signatures of large-scale soil moisture dynamics on streamflow statistics across U.S. climate regimes. *Water Resour Res* 43(11):W11413.
5. Botter G, Basso S, Porporato A, Rodriguez-Iturbe I, Rinaldo A (2010) Natural streamflow regime alterations: Damming of the Piave river basin (Italy). *Water Resour Res* 46 (6):W06522.
6. Rodriguez-Iturbe I, Porporato A (2004) *Eco-Hydrology of Water Controlled Ecosystems* (Cambridge Univ Press, Cambridge, UK).
7. Brutsaert W, Nieber JL (1977) Regionalized drought flow hydrographs from a mature glaciated plateau. *Water Resour Res* 13(3):637–643.
8. Botter G (2010) Stochastic recession rates and the probabilistic structure of stream flows. *Water Resour Res* 46(12):W12527.

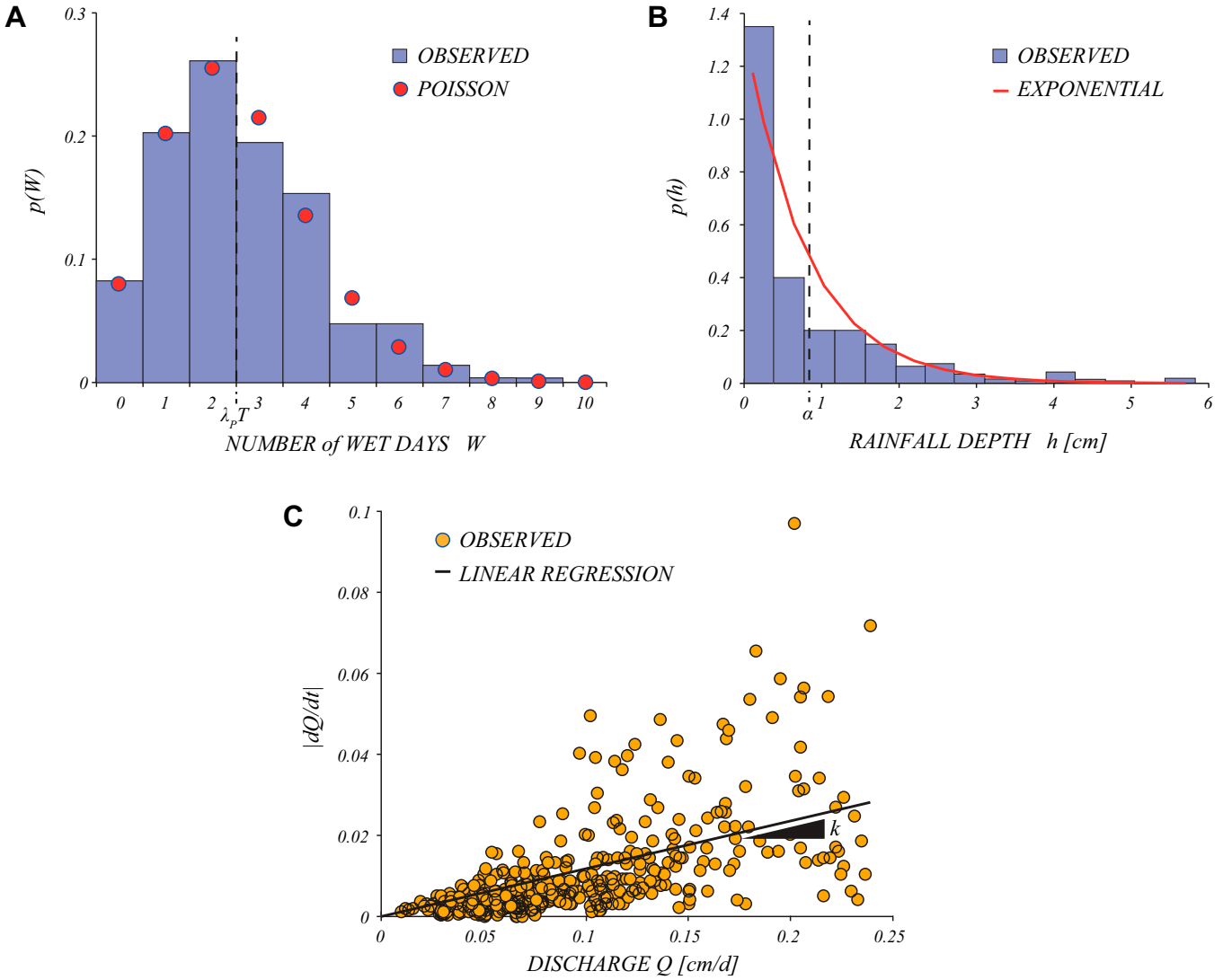

Fig. S1. Parameter identification. (*A*) Comparison between the pdf of the number of rainy days p(W) in a reference time span, T = 10 d, observed at the gauging station of Jackson Springs during the spring from 1985 to 1992 (histogram) and the corresponding Poisson distribution assumed by the analytical model (red dots). The vertical dashed line indicates the mean number of wet days within the reference time period, λ_pT. (*B*) Comparison between the distribution of the daily rainfall depths p(h) observed at the gauging station of Jackson Springs during the spring from 1985 to 1992 (histogram) and the exponential distribution assumed by the analytical model (red solid line). The mean rainfall depth, α, is also indicated (vertical dashed line). (*C*) Regression analysis of the streamflows observed in Drowning Creek during the spring season of the years 2001–2008. The flow decay rate, *k*, is derived from observed streamflows by a linear regression of the estimated temporal derivatives of *Q* (*dQ*/*dt*) plotted vs. the corresponding observed discharges *Q* (6).

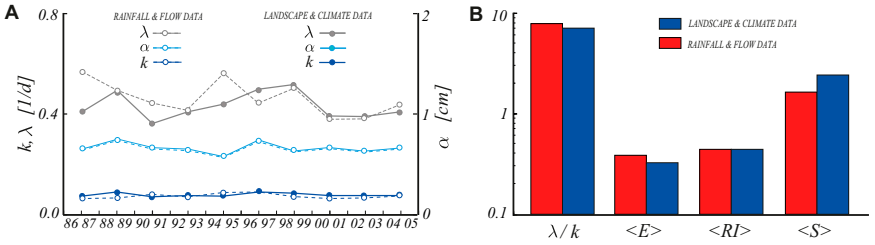

Fig. S2. Comparison of model parameter estimates using different methods. (*A*) Temporal evolution of the parameters λ, *k*, and α estimated based on climate and landscape information (solid lines) compared with the corresponding estimate made using rainfall and streamflow data (dashed lines) for the Boite catchment at Cancia. (*B*) Comparison between the estimates of λ/*k*, *E*, the *RI*, and sensitivity (*S*), which result from the use of rainfall and streamflow data (red histograms), and the corresponding values estimated based on climatic and landscape data (blue histograms).

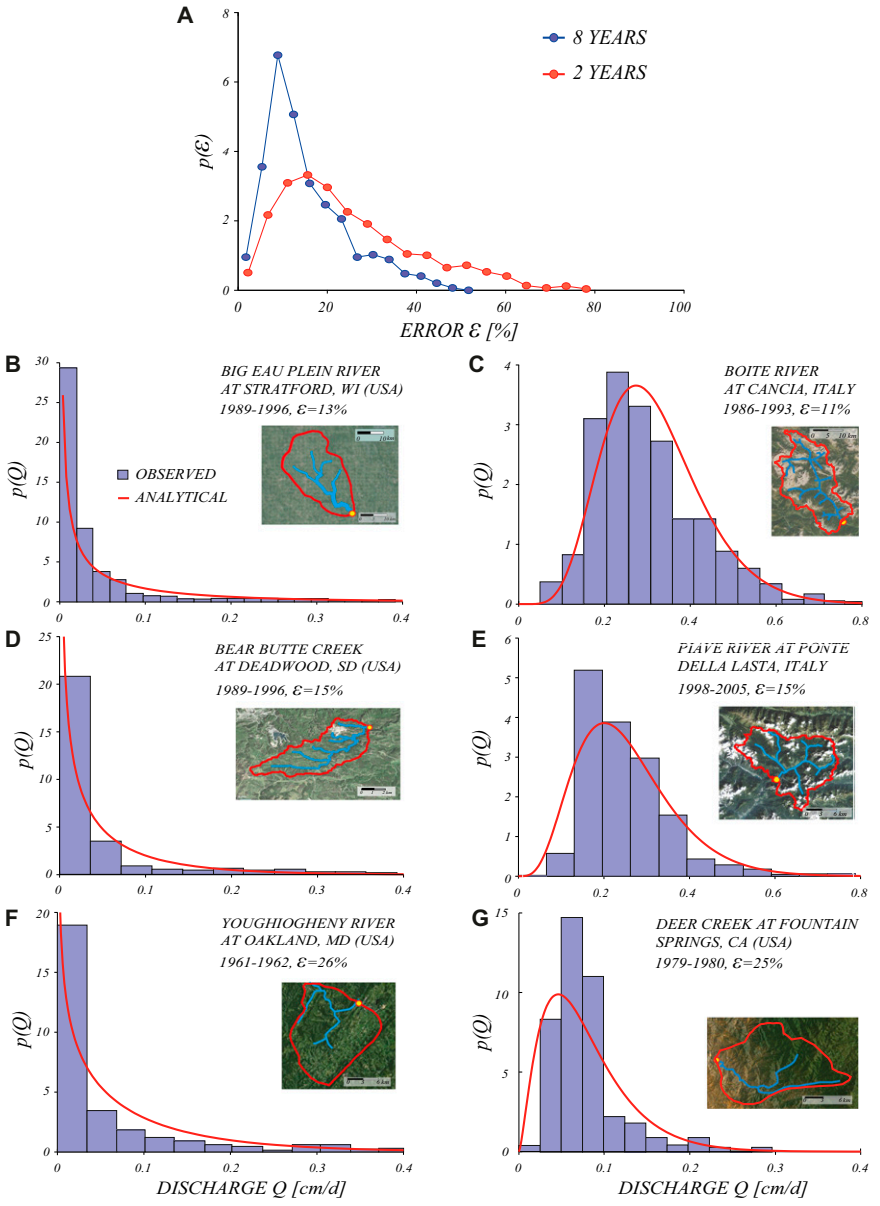

Fig. S3. Model performances. (*A*) Frequency distribution of the error estimated for all the combinations of catchments/seasons and for all the available nonoverlapping periods of 2 and 8 y contained within each dataset. (*B*–*G*) Comparison between the observed streamflow distributions (histograms) and the corresponding estimates of $p(Q)$ provided by the analytical model (red lines) for selected combinations of catchments/seasons and different time scales (2-y and 8-y regimes). (*B*) Fall streamflow regime of the Big Eau Pleine River at Stratford from 1989 to 1996. (*C*) Summer streamflow regime of the Boite River at Cancia from 1986 to 1993. (*D*) Summer streamflow regime of the Bear Butte Creek at Deadwood from 1989 to 1996. (*E*) Summer streamflow regime of the Piave River at Ponte della Lasta from 1998 to 2005. (*F*) Fall streamflow regime of the Youghiogheny River at Oakland from 1961 to 1962. (*G*) Spring streamflow regime of the Deer Creek at Fountain Springs from 1979 to 1980.

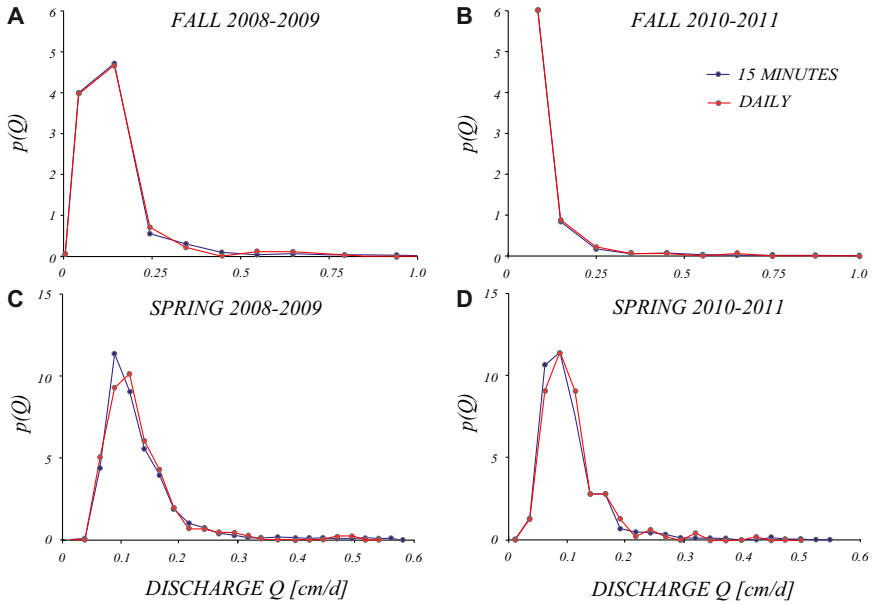

Fig. S4. Daily and 15-min streamflow distributions in the Flat Creek (NC) during the fall (*A* and *B*) and the spring (*C* and *D*), evaluated during two different time periods (2008–2009 and 2010–2011).

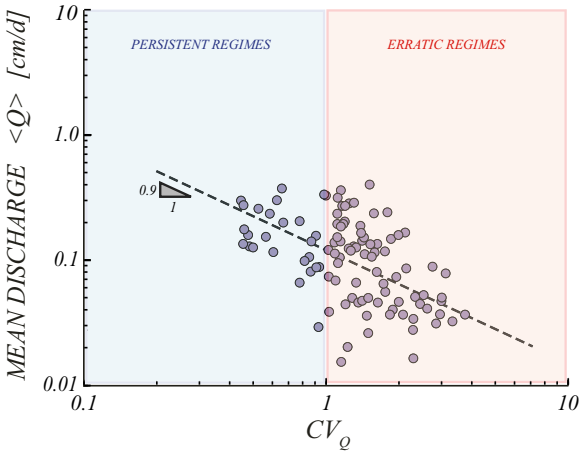

Fig. S5. Anticorrelation between mean specific discharge and intraseasonal flow variability. Mean specific (per unit area) discharge, plotted as a function of the CV_Q for each available combination of catchments/seasons. The dashed line indicates the least-squared regression (slope = 0.9, $r^2 = 0.3$). The plot suggests that erratic regimes are infrequent in rivers with high specific discharges.

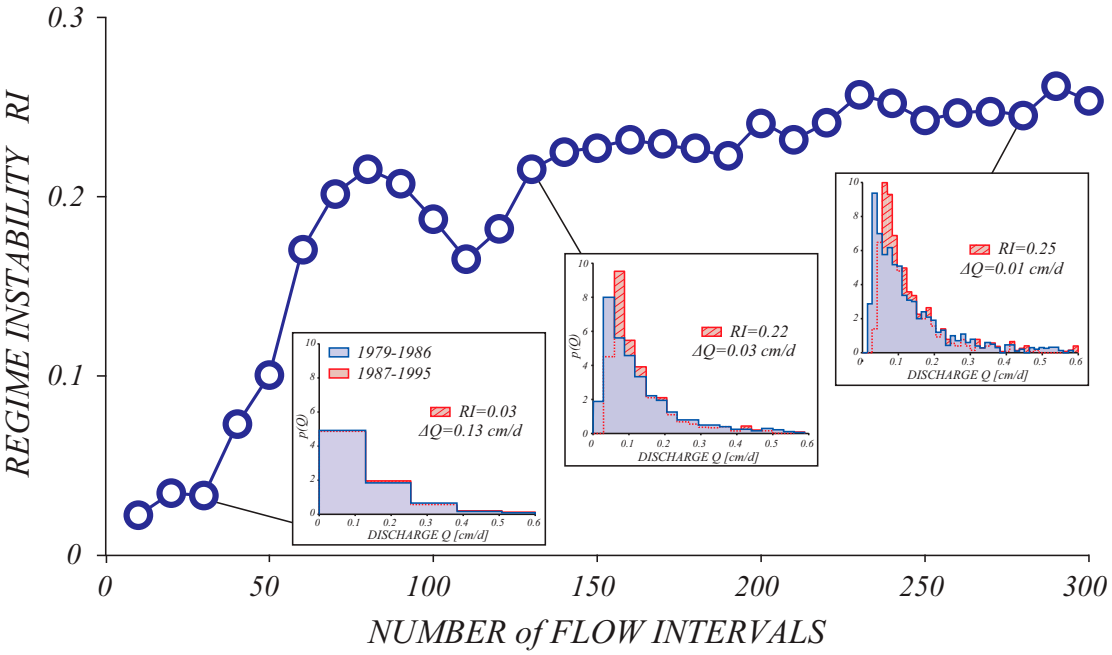

Fig. S6. Computation of the regime instability. Springtime *RI* observed between the periods 1979–1986 and 1987–1994 in the Rivanna River as a function of the number of flow intervals, *N*, used to compute the streamflow probability distributions (Eq. **S6**). (*Left Inset*) When *N* is small, the *RI* is artificially small because of the enhanced smoothing of the estimated pdf. (*Right Inset*) On the contrary, when too many intervals are used, the *RI* is artificially large because of the increased number of intersections between the two pdf estimates produced by their enhanced fluctuations. (*Middle Inset*) Presence of a plateau in the function *RI*(*N*) allows one to single out the proper value for the regime instability between the considered periods.

Table S1. Summary information about the 44 catchments selected in this study

Catchment	State (country)	Area, km^2	Period	Streamflow gauging station (state)	Rainfall gauging stations (state)	Seasons
Valley Creek	Alabama (United States)	383	1978–2012	Oak Grove (AL)	Bankhead Lock and Dam (AL)	Spring, summer, autumn, winter
Banning Creek	Arizona (United States)	23	2005–2011	Bisbee (AZ)	Bisbee (AZ)	Summer
Boulder Creek	Arizona (United States)	98	1984–1993	Rock Springs (AZ)	Crown King (AZ)	Spring
South Fork Parker Creek	Arizona (United States)	3	1986–2012	Roosevelt (AZ)	Workman Creek (AZ)	Spring
White River	Arkansas (United States)	1,036	1963–2003	Fayetteville (AR)	Fayetteville (AR)	Spring, summer, autumn, winter
Deer Creek	California (United States)	216	1969–2012	Fountain Springs (CA)	Glennville (CA)	Spring, summer, autumn, winter
Vallecito Creek	Colorado (United States)	188	1963–1997	Bayfield (CO)	Pagosa Springs (CO)	Autumn
Prairie Creek	Florida (United States)	603	1977–2012	Fort Ogden (FL)	Arcadia (FL)	Spring, summer, autumn, winter
Mississinewa River	Indiana (United States)	1,766	1931–2012	Marion (IN)	Marion (IN)	Spring, summer, autumn
Little Sandy River	Kentucky (United States)	1,036	1969–2001	Grayson (KY)	Grayson (KY)	Spring, summer, autumn, winter
Little Androscoggin River	Maine (United States)	190	1978–2003	South Paris (ME)	West Paris (ME)	Spring, summer, autumn, winter
Youghiogheny River	Maryland (United States)	347	1941–2012	Oakland (MD)	Oakland (MD)	Spring, summer, autumn, winter
West Swan River	Minnesota (United States)	42	1963–1979	Silica (MN)	Hibbing (MN)	Spring, summer, autumn
Castor River	Missouri (United States)	1,096	1936–1991	Zalma (MO)	Zalma (MO)	Spring, summer, autumn, winter
Salt Creek	Nebraska (United States)	433	1953–2002	Roca (NE)	Roca (NE)	Spring, summer, autumn
Gallinas Creek	New Mexico (United States)	218	1990–1999	Montezuma (NM)	Wesner Springs (NM)	Summer, autumn
Rio Nutria	New Mexico (United States)	185	1972–1995	Ramah (NM)	McGaffey (NM)	Spring
Drowning Creek	North Carolina (United States)	474	1952–2012	Hoffmann (NC)	Jackson Springs (NC)	Spring, summer, autumn, winter
Flat Creek	North Carolina (United States)	20	1989–2012	Inverness (NC)	Inverness (NC)	Spring, summer, autumn, winter
Indian Creek	North Carolina (United States)	179	1953–2012	Laboratory (NC)	Lincolnton (NC)	Spring, summer, autumn, winter
Jacob Fork	North Carolina (United States)	67	1961–2012	Ramsey (NC)	Casar (NC)	Spring, summer, autumn, winter
Lookingglass Creek	Oregon (United States)	409	1955–1998	Brockway (OR)	Reston (OR)	Spring, summer, autumn, winter
Bear Butte Creek	South Dakota (United States)	43	1988–2011	Deadwood (SD)	Deadwood (SD)	Spring, summer
Spring Creek	South Dakota (United States)	159	1983–1993	Flandreau (SD)	Flandreau (SD)	Spring, summer, autumn
Cowhouse Creek	Texas (United States)	1,178	1992–2007	Pidcoke (TX)	Pidcoke (TX)	Spring, summer, autumn, winter
Redgate Creek	Texas (United States)	45	1962–2012	Columbus (TX)	Columbus (TX)	Spring, summer, autumn, winter
Santa Clara River	Utah (United States)	48	2005–2012	Pine Valley (UT)	Gardner Peak (UT)	Summer
Rivanna River	Virginia (United States)	1,717	1947–2012	Palmyra (VA)	Charlottesville (VA)	Spring, summer, autumn, winter
Rock Creek	Washington (United States)	64	1944–1971	Cedarville (WA)	Elma (WA)	Spring, summer, autumn, winter
Sand Run	West Virginia (United States)	37	1946–2012	Buckhannon (WV)	Buckhannon (WV)	Spring, summer, autumn, winter
Big Eau Pleine River	Wisconsin (United States)	580	1949–2012	Stratford (WI)	Stratford (WI)	Spring, summer, autumn
Shell Creek	Wyoming (United States)	376	1980–2011	Shell (WY)	Shell Creek (WY)	Summer
Brenta	Italy	214	1995–2010	Borgo Valsugana	Vetriolo, Canezza, Levico, Telve di Sopra, Rifugio Crucolo	Summer
Brenta	Italy	766	1995–2010	Ponte Filippini	Vetriolo, Canezza, Levico, Telve di Sopra, Rifugio Crucolo, Longana	Summer
Boite	Italy	82	1992–2008	Podestagno	Podestagno	Summer

Table S1. Cont.

Catchment	State (country)	Area, km^2	Period	Streamflow gauging station (state)	Rainfall gauging stations (state)	Seasons
Boite	Italy	313	1986–2008	Cancia	Podestagno, Faloria, Borca, Cortina	Summer
Cordevole	Italy	8	1985–2008	La Vizza	Passo Pordoi	Summer
Cordevole	Italy	109	1990–2008	Saviner	Passo Pordoi, Arabba, Passo Falzarego	Summer
Fersina	Italy	78	1996–2010	Canezza	Canezza	Summer
Fersina	Italy	175	1996–2006	Trento	Trento Roncafort, Canezza	Summer
Fiorentina	Italy	58	1993–2008	Sottorovei	Passo Falzarego, Caprile, Pescul	Summer
Padola	Italy	130	1987–2007	Santo Stefano di Cadore	Passo Monte Croce Comelico, Casamazzagno	Summer
Piave	Italy	355	1990–2006	Ponte della Lasta	Passo Monte Croce Comelico, Malga Campobon, Santo Stefano di Cadore, Casamazzagno, Costalta, Cimacanale, Sappada	Summer
Sonna	Italy	120	1986–2007	Feltre	Monte Avena, Feltre	Summer